



HAL
open science

4f spin driven ferroelectric-ferromagnetic multiferroicity in PrMn₂O₅ under a magnetic field

S. Chattopadhyay, V. Balédent, S. K. Panda, Sh. Yamamoto, F. Duc, T. Herrmannsdörfer, M. Uhlarz, T. Gottschall, O. Mathon, Z. Wang, et al.

► **To cite this version:**

S. Chattopadhyay, V. Balédent, S. K. Panda, Sh. Yamamoto, F. Duc, et al. 4f spin driven ferroelectric-ferromagnetic multiferroicity in PrMn₂O₅ under a magnetic field. *Physical Review B*, 2020, 102, pp.094408. 10.1103/PhysRevB.102.094408 . hal-03022065

HAL Id: hal-03022065

<https://hal.science/hal-03022065>

Submitted on 9 Dec 2020

HAL is a multi-disciplinary open access archive for the deposit and dissemination of scientific research documents, whether they are published or not. The documents may come from teaching and research institutions in France or abroad, or from public or private research centers.

L'archive ouverte pluridisciplinaire **HAL**, est destinée au dépôt et à la diffusion de documents scientifiques de niveau recherche, publiés ou non, émanant des établissements d'enseignement et de recherche français ou étrangers, des laboratoires publics ou privés.

4*f*-spin driven ferroelectric-ferromagnetic multiferroicity in PrMn₂O₅ under magnetic field

S. Chattopadhyay,^{1,*} V. Balédent,² S. K. Panda,³ Sh. Yamamoto,¹ F. Duc,⁴ T. Herrmannsdörfer,¹ M. Uhlarz,¹ T. Gottschall,¹ O. Mathon,⁵ Z. Wang,⁶ C. Strohm,⁷ M. Greenblatt,⁸ P. Foury-Leylekian,² and J. Wosnitzer^{1,9}

¹*Dresden High Magnetic Field Laboratory (HLD-EMFL) and Würzburg-Dresden Cluster of Excellence ct.qmat, Helmholtz-Zentrum Dresden-Rossendorf, 01328 Dresden, Germany*

²*Université Paris-Saclay, CNRS, Laboratoire de Physique des Solides, 91405, Orsay, France*

³*Department of Physics, Bennett University, Greater Noida 201310, Uttar Pradesh, India*

⁴*Laboratoire National des Champs Magnétiques Intenses (LNCMI-EMFL, UPR 3228 CNRS, INSA, UGA, UPS) 143 avenue de Ranguel, F-31400 Toulouse, France*

⁵*European Synchrotron Radiation Facility, B.P. 220, 38043 Grenoble, France*

⁶*Anhui Province Key Laboratory of Condensed Matter Physics at Extreme Conditions, High Magnetic Field Laboratory of the Chinese Academy of Sciences, Hefei 230031, China*

⁷*Deutsches Elektronen-Synchrotron DESY, 22607 Hamburg, Germany*

⁸*Department of Chemistry and Chemical Biology, Rutgers,*

The State University of New Jersey, Piscataway, New Jersey 08854, USA

⁹*Institut für Festkörper- und Materialphysik, Technische Universität Dresden, 01062 Dresden, Germany*

(Dated: August 28, 2020)

In contrast to all other members of the RMn₂O₅ family with non-zero 4*f* electrons (*R* = Nd to Lu), PrMn₂O₅ does not show any spin-driven ferroelectricity in the magnetically ordered phase. By means of high-field electric polarization measurements up to 45 T, we have found that this exceptional candidate undergoes a spin-driven multiferroic phase under magnetic field. X-ray magnetic circular dichroism studies up to 30 T at the Pr *L*₂-edge show that this ferroelectricity originates from and directly couples to the ferromagnetic component of the Pr³⁺ spins. Experimental observations along with our GGA+U calculations reveal that this exotic ferroelectric-ferromagnetic combination stabilizes through the exchange-striction mechanism solely driven by a 3*d*-4*f* type coupling, as opposed to the other RMn₂O₅ members with 3*d*-3*d* driven ferroelectric-antiferromagnetic type conventional type-II multiferroicity.

I. INTRODUCTION

The research on functional materials, aiming at the next generation of smart devices, witnessed a massive upturn after the advent of materials showing multiple combined properties. Among such materials, an intriguing family of compounds known as magnetoelectric multiferroics (MEMF) with strongly coupled magnetism and ferroelectricity has attracted special attention¹⁻³. For the MEMF family, reasons for being so highly sought after are twofold: (i) The microscopic origin of the magnetoelectric coupling is of fundamental interests that fascinates the condensed-matter community and (ii) from an applied perspective, the spintronics and data-storage technologies would greatly benefit from such functionalities.

However, to be well suited for device-applications, in addition to the room temperature functionality, MEMF materials are expected to fulfill two very important criteria: the coexistence of ferromagnetism with ferroelectricity and a strong coupling between the two order parameters. In reality, it is extremely difficult to satisfy both criteria simultaneously and only a few single-phase materials are known to show coupling between the ferroelectric and ferromagnetic component⁴⁻⁶. There are also a few theoretical works proposing strategies to couple ferroelectricity with weak ferromagnetism in a material^{7,8}.

Multiferroic materials have been classified into two types. In type-I materials, ferroelectricity and magnetism have different origins. Whereas in type-II multiferroics, spin-driven ferroelectricity is caused by magnetic ordering itself, resulting an intrinsically strong magnetoelectric coupling^{3,9,10}. However,

the magnetism being frustrated in character, type-II multiferroics show the coexistence of complex antiferromagnetism and ferroelectricity. As multiferroics are relatively scarce, an important research activity focused on heterostructures with stacked ferromagnetic and ferroelectric layers³. However, as this eventually leads to type-I artificial multiferroics, the disadvantage of usually having small-coupling remains unsolved.

In this context, studies on RMn₂O₅ (*R* = Bi, rare-earth) oxides are particularly interesting. The RMn₂O₅ family is known for showing a series of magnetic transitions starting from *R* = Nd to Lu. The first magnetic transition around 40±5 K to an incommensurate antiferromagnetic (AF) state is followed by a second transition leading to a commensurate AF ordering of the Mn spins. An electric polarization (*P*) emerges either with the first (*R* = Tb, Sm, Nd) or the second magnetic transition along the *b* axis, asserting the type-II character of the multiferroicity¹¹⁻²⁰. The associated strong coupling has been reported for GdMn₂O₅ and TbMn₂O₅ where the electric polarization (*P*) can even be reversed by applying a modest magnetic field of a few Tesla^{1,2,21,22}. With lowering the temperature, a third magnetic transition generally appears stabilizing another incommensurate AF order.

Neutron diffraction studies indicate that this spin-driven ferroelectricity is in general a consequence of a quasi-collinear ordering of the Mn spins (either Mn³⁺ sublattice or both Mn³⁺ and Mn⁴⁺ sublattices)^{11,12,14}. We note that, although the actual room-temperature crystal structure of RMn₂O₅ is already polar with a *Pm* (monoclinic) space group²³, the structural distortion with respect to the average non-polar *Pbam*

space group^{24,25} is so small that the induced polarization becomes extremely weak and cannot be measured directly in this regime. We will thus neglect this weak symmetry breaking in the following.

In RMn_2O_5 , the long-standing debate on the microscopic origin of the spin-driven ferroelectricity has been resolved recently confirming Mn-Mn exchange-striction to be the responsible one¹². This result portrays the dominant role of the $3d$ ions and their frustrated superexchange interactions in the emergence of the spin-driven ferroelectricity. Although known for a few other multiferroics,^{4,6,26} in RMn_2O_5 , the role of the $4f$ ions has only been revealed recently to explain the magnetoelectric behaviors in some candidates^{27,28}. Particularly in $GdMn_2O_5$ and $NdMn_2O_5$, in addition to the dominant $3d$ - $3d$ effect, a weak $3d$ - $4f$ interaction was proposed to explain the observed spin-driven ferroelectricity^{15,29}.

Among all compositions, $PrMn_2O_5$ appears to be an outstanding exception. In contrast to the other RMn_2O_5 members with non-zero numbers of $4f$ electrons, $PrMn_2O_5$ does not show any spin-driven ferroelectricity. Powder neutron diffraction measurements show that Mn^{3+} moments order at $T_{N1} = 25$ K, following a magnetic propagation vector $q_1 = (0.5, 0, 0)$. With decreasing temperature, Mn^{4+} ordering appears at $T_{N2} = 18$ K with $q_2 = (0, 0, 0.5)$ ³⁰. Such distinct orderings of the Mn^{3+} and Mn^{4+} ions are indicative of a very weak exchange coupling between the two sublattices, explaining the absence of ferroelectricity. Pr^{3+} sublattice does not fully order down to 1.5 K. Only a partial ordering of Pr^{3+} below T_{N1} was reported³⁰ suggesting a coupling between Mn^{3+} and Pr^{3+} . A powder neutron study under high pressure (a few GPa) shows the emergence of a collinear magnetic phase favorable for spin-driven ferroelectricity³¹. However, electric polarization measurements were not possible to perform at this pressure regime to probe the possible onset of multiferroicity directly.

In this work, we report the emergence of a multiferroic phase under magnetic field in $PrMn_2O_5$. Using the combination of high-field electric polarization, x-ray magnetic circular dichroism (XMCD), and density functional theory (DFT) based calculations, we show that unlike the multiferroicity observed in other RMn_2O_5 members, the spin-driven ferroelectricity in $PrMn_2O_5$ originates from and couples to a ferromagnetic component. Moreover, the associated mechanism involved is no longer based on the $3d$ - $3d$ coupling, rather the spin-driven ferroelectricity is solely a manifestation of $3d$ - $4f$ exchange interaction.

As mentioned, the presence of coupled ferroelectric and ferromagnetic components is very rare to find. In addition to that, $PrMn_2O_5$ hosts $3d$ - $4f$ coupling and exchange-striction mechanism as well. As separate phenomena, these features have been observed. However, to have a material like $PrMn_2O_5$, which hosts simultaneous presence of all of these effects/mechanisms is rather unique to our knowledge.

Single crystals of $PrMn_2O_5$ from the same batch as mentioned in reference²³ were used for this study. The crystals were grown using electrolysis method as described in references^{32,33}. The as-grown crystals have a thin plate-like morphology with the plate-surface being perpendicular to the b -axis.

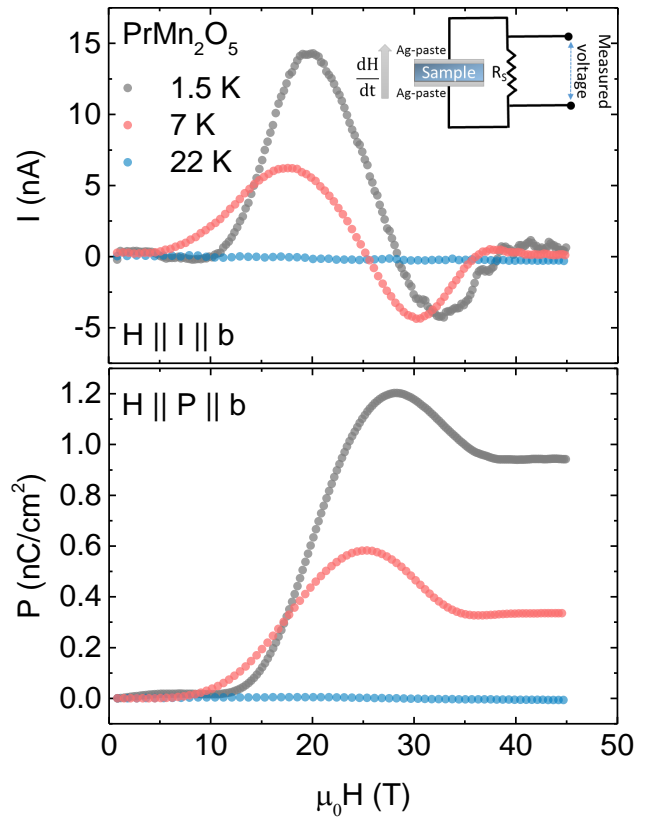


FIG. 1. Top panel shows magnetic field (H) dependence of the pyrocurrent (I) up to 45 T at different temperatures using $H \parallel I \parallel b$ configuration. Inset shows schematic diagram of the pyroelectric technique used to record the field dependence of the pyroelectric applying pulsed magnetic fields. Bottom panel depicts electric polarization (P) along the b axis as a function of magnetic field.

II. RESULTS & DISCUSSION

A. High-field Electric Polarization & Magnetization

We carried out magnetic-field-dependent electric-polarization (P) measurements up to 45 T using a pyroelectric technique at the Dresden High Magnetic Field Laboratory (HLD-EMFL). Field pulses of ~ 20 ms duration were applied along b to measure the spin-induced pyroelectric current (I) along the same direction. A schematic diagram of the measurement technique is shown in the inset of the top panel of Fig. 1. Since the sweep rate of the magnetic field (dH/dt) is large in pulsed-field, the dP/dt and hence the pyroelectric-current becomes detectable even for a small change in P . The field induced pyrocurrent (I) was recorded by measuring the voltage variation across a shunt resistor (R_S). This shunt resistor was connected in series with the measurement circuit by a digital oscilloscope (Yokogawa DL750). The oscilloscope was operated with a high sampling rate of 1 MSs^{-1} and a resolution of 16 bit. The top panel of Fig. 1 shows the field dependence of I measured at 1.5 K, 7 K, and 22 K. The electric polarization was then calculated

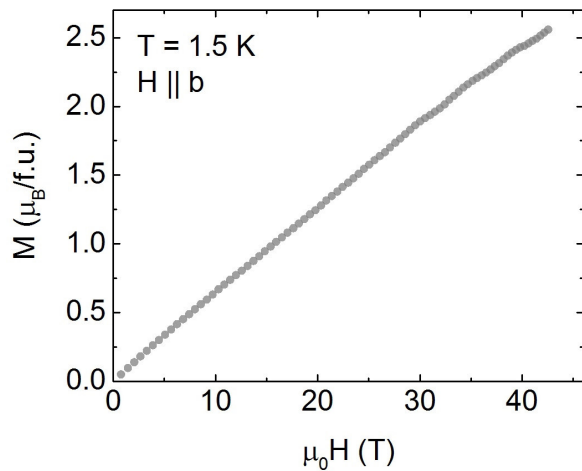


FIG. 2. Field dependence (H) of the magnetization (M) up to 42 T at 1.5 K with $H \parallel b$.

by integrating the $I(H)$ curves. The reproducibility of the data was verified carefully by repeating the measurements multiple times.

From the $P(H)$ data shown in the bottom panel of Fig. 1, it is evident that at 1.5 K, an electric polarization emerges above ~ 12 T along the b direction. P increases with H and attains a maximum around 27 T. With further increase in field, P decreases slowly and finally enters to a flat region above 35 T. Notably, the polarization amplitude in PrMn_2O_5 (~ 1 nC/cm²) is of the same order as found in NdMn_2O_5 , the adjacent member. The polarization gradually becomes weaker at higher temperatures and finally vanishes in the paramagnetic regime.

We also performed high-field magnetization measurements using pulsed magnetic fields at the HLD. Similar to the polarization measurements, the pulse duration was ~ 20 ms. We repeated this measurement a few times to ensure the reproducibility of the data. Figure 2 shows $M(H)$ data measured at 1.5 K up to 42 T with H applied parallel to the b direction. In contrast to the polarization data, no anomaly is seen in $M(H)$ over the entire field range. The magnetization does not show any indication of saturation even at the highest field measured. In this system, the overall magnetization is dominated by the Mn moments. Therefore, the observed dissimilarities between the field dependence of the polarization and magnetization indicate that the magnetic-field-driven ferroelectricity does not seem to involve $3d$ ions directly. Rather, it indicates a possible $4f$ ion involvement in this case.

B. High-Field X-Ray-Magnetic-Circular-Dichroism

In order to investigate the effect of a strong magnetic field on the rare-earth ordering, we performed x-ray-magnetic-circular-dichroism (XMCD) measurements. The high-field XMCD measurements at the $\text{Pr-}L_2$ edge were performed at the energy dispersive x-ray absorption spectroscopy beamline ID24 at ESRF, Grenoble³⁴. The pulsed-field magnet used for this purpose was connected to a 1.15 MJ portable power sup-

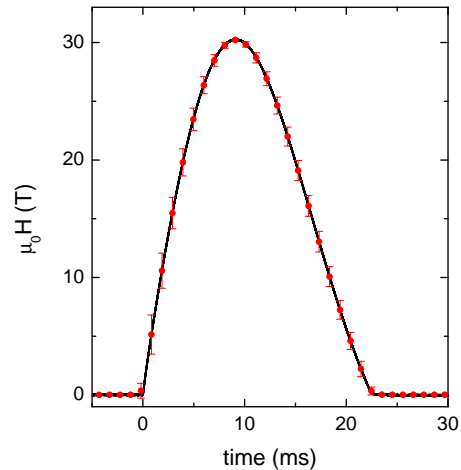


FIG. 3. Time profile of the magnetic field pulse used for the x-ray magnetic circular dichroism measurements. The red symbols correspond to the average values of the magnetic field and error bars over a series of 10 pulses for each data-acquisition window of 1 ms.

ply developed at the LNCMI-Toulouse. The magnet produces a maximum field of ~ 30 T with a rise time of ~ 10 ms and a total duration of ~ 23 ms (Fig. 3) in every 8 min^{35–37}. Figure 4(a) shows a representative x-ray absorption spectrum (XAS) recorded at the $\text{Pr-}L_2$ edge at 2 K. XMCD spectra were obtained in transmission mode at 2 K as the difference of x-ray absorption spectra when changing the field direction ($+b$ and $-b$ directions). The same measurement protocol was applied for both right- and left-handed circularly polarized x-ray beams. To record the field dependence of the absorption spectrum, a multi-frame acquisition scheme with high-frame-rate detector FReLoN (Fast-Readout Low Noise) was used and a series of 50 full-energy spectra (i.e., acquisition windows of 1 ms) were recorded during each field pulse³⁸. For our purpose, the crystal was mounted with the b axis parallel to the magnetic field and incident beam direction. The polished sample (thinned down to ~ 15 μm) was sandwiched between two diamond windows. This assembly was mounted in a dynamic He-flow cryostat in which the sample was cooled down through forced convection.

Figure 4(b) shows XMCD spectra recorded at magnetic fields between ~ 4.6 T and ~ 30 T. The data presented here is a summation of 16 field-pulses to improve the signal-to-noise ratio. The main contribution at the L_2 edge comes from the $2p_{1/2} \rightarrow 5d_{3/2}$ dipole transition according to the selection rules. As the magnetic field increases, the XMCD amplitude becomes more pronounced. The observed x-ray absorption spectra and dichroic spectra at the high-field regime are consistent with those reported for other Pr^{3+} -based compounds ($4f^2$)^{39,40}.

The dichroic signal starts to appear about 10 T, reaches its maximum around 27 T, and then drops gradually with further increase in H . Although we cannot entirely exclude a contribution from the Mn ions, the $\text{Pr-}L_2$ edge XMCD signal observed in PrMn_2O_5 is mainly caused by the Pr spins. The direct evidence can be seen from the peak shape of the

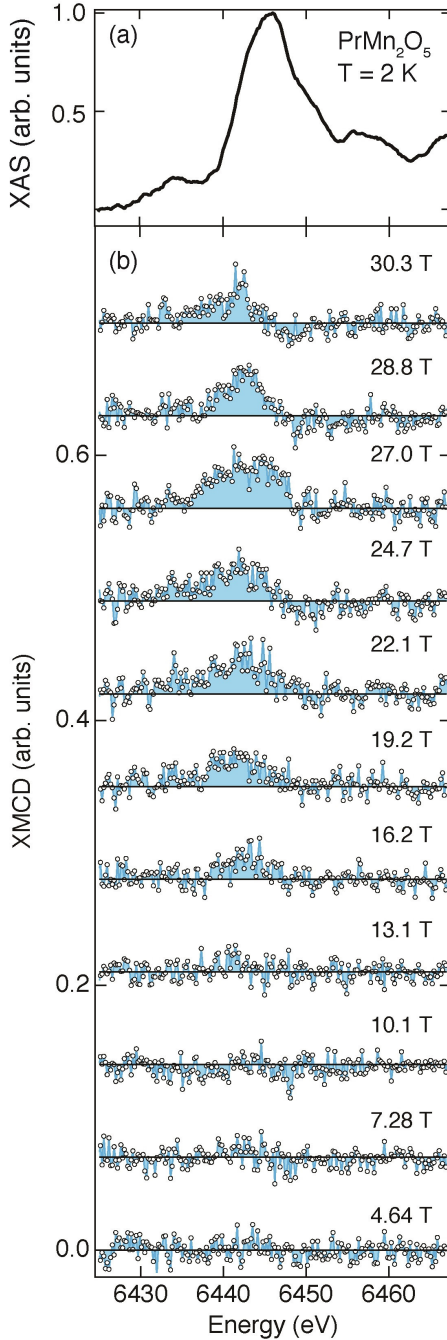


FIG. 4. (a) X-ray absorption spectrum (XAS) and (b) x-ray magnetic circular dichroism (XMCD) spectra at the Pr L_2 -edge for PrMn_2O_5 with magnetic field applied parallel to the b -axis at $T = 2$ K. Data sets for different magnetic fields are offset along the vertical axis for clarity.

XMCD signal. It does not change with field, only its amplitude gets modified unlike garnet oxides,^{41,42} where the L edge XMCD line shape as well as the amplitude change with field due to contributions of comparable strength from both $4f$ and $3d$ ions. In case of intermetallic compounds composed of a $4f$ rare-earth and a $3d$ transition-metal, earlier study reported

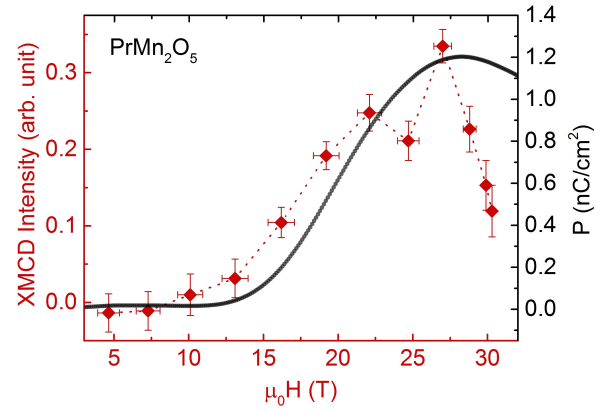


FIG. 5. Field dependence of the XMCD integrated intensity over the entire Pr- L_2 edge range at 2 K compared with the field dependence of the electric polarization along the b axis at $T = 1.5$ K shown in Fig. 4. The dotted line is a guide to the eyes.

a sizable transition-metal contribution as well to the rare-earth L_2 edge⁴³. This is because the $3d$ - $4f$ exchange interaction in such intermetallic compounds is mediated by the rare-earth $5d$ band which is directly accessed by the rare-earth L edge. Instead, in our system, the weaker super-exchange $3d$ - $4f$ interaction is mediated via the oxygen $2p$ state, which results in a marginal transition-metal contribution to the XMCD signals at the rare-earth L edges. Here, the mixed $4f$ - $5d$ state of Pr^{3+} is the reason the transition toward $5d_{3/2}$ gives access to the $4f$ spin's ferromagnetic ordering. As a consequence, these results prove that the Pr ions contain a ferromagnetic component along the b axis under an external magnetic field applied along the same direction.

Notably, the field dependence of the integrated XMCD signal has a remarkable resemblance with the aforementioned polarization curve. In Fig. 5 we show the field dependence of both integrated XMCD signal and polarization at comparable temperatures (2 K for XMCD and 1.5 K for P). The error bars shown are standard deviations extracted from averaging procedure for 16-polarization-dependent spectra. The similarity between both quantities suggests that the two order parameters are coupled. The direct consequence is that PrMn_2O_5 becomes a type-II multiferroic under magnetic field with coupled ferromagnetism and ferroelectricity. Above ~ 27 T, the steeper decrease of the XMCD integrated intensity as compared to the $P(H)$ behavior might come from the fact that the fluctuations of the signal at high magnetic field are larger, as reflected through the larger error bars when approaching 30 T. Therefore, the slope of the curve should be taken as an overall trend of the field dependence without considering it with high precision.

C. Density-Functional-Theory Calculations

In order to provide further credence to our experimental findings, the density-functional-theory (DFT) calculations were performed in the generalized-gradient-approximation +

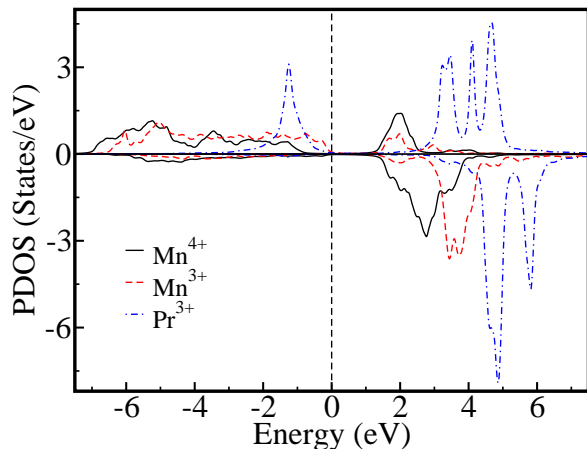


FIG. 6. Theoretically calculated partial density of states for Pr-*f* and Mn-*d* in the magnetic ground state.

Hubbard U (GGA+ U) approach by means of a full potential linearized muffin-tin (MT) orbital method (FP-LMTO)^{44,45} as implemented in the RSPt code⁴⁶. The Brillouin-zone (BZ) integration is carried out by using the thermal smearing method in a $8 \times 7 \times 10$ k-mesh which corresponds to 560 k-points in the irreducible part of the BZ. For the charge density and potential angular decomposition inside the MT spheres, the value of maximum angular momentum was taken equal to $l_{\max} = 8$. To describe the electron-electron correlation within the GGA+ U approach, we used $U = 4$ eV and $J = 0.8$ eV for the Mn-*d* states and $U = 5$ eV and $J = 0.5$ eV for the Pr-*f* states.

The calculated projected density of the states (PDOS) are displayed in Fig. 6 which shows that the system is insulating with a gap of 1.2 eV. As expected, the Pr-*f* states are highly localized. We observe that the majority spin channel of Pr-*f* states shows a valence band peak at around -1.3 eV binding energy and rest of the states appear above the Fermi level between 3 to 5 eV, while the minority spin channel is completely empty. Both the spin moment on the Pr-site and the projected density of states are consistent with the nominal $4f^2$ state of the Pr ion. On the other hand, the occupied Mn-*d* states are fairly delocalized within the binding energy range from -7 eV to the Fermi level. For both Mn⁴⁺ and Mn³⁺ ions, the majority channel is partially filled, while the minority channel is completely empty. The PDOS and the projected moments are consistent with the tetravalent ($3d^3$) and trivalent ($3d^4$) states of Mn⁴⁺ and Mn³⁺, respectively.

The obtained spin and orbital angular momentum of the Pr³⁺ ions are $1.81 \mu_B$ and $1.99 \mu_B$, respectively and they are in opposite directions. The spin moment on Pr³⁺ is large as expected from the nominal charge state (f^2). However, the presence of a strong reverse orbital moment makes the net moment very small ($0.18 \mu_B$). It provides the explanation for the observed low moments on Pr site in neutron experiments ($\sim 0.5 \mu_B/\text{Pr}^{3+}$)³⁰. The moment of Mn³⁺ and Mn⁴⁺ are essentially spin moments with the estimated values 3.38 and $2.55 \mu_B$, respectively.

Further, to establish a spin model to understand the field

dependence of the electric polarization and its relation with the long range magnetic ordering, we estimated the inter-atomic magnetic exchange interactions from the converged GGA+ U calculations using the formalism of Ref.⁴⁷. We used the magnetic-force theorem^{48,49} to extract the effective inter-site exchange parameters (J_{ij}). In this method, we mapped the total converged energies of the magnetic system onto the following Heisenberg-type spin Hamiltonian

$$\hat{H} = - \sum_{i \neq j} J_{ij} \vec{S}_i \cdot \vec{S}_j. \quad (1)$$

Here, the indices i and j span over the positions of the intrinsically magnetic ions, i.e. Pr³⁺, Mn³⁺, and Mn⁴⁺. The effective J_{ij} is extracted in a linear-response manner via a Green's function technique. A detailed discussion of the implementation of the magnetic force theorem in RSPt is provided in Ref.⁵⁰. All the calculations are carried out using the structural parameters given in Ref.³⁰. The magnetic structure determination from neutron diffraction data shows that the magnetic moments of Pr³⁺ are parallel to their nearest-neighbour Mn³⁺ spins and they make only a small angle with respect to the a axis. Therefore, in the first approximation, we can safely ignore the anisotropic terms in the spin-Hamiltonian. That is precisely the reason, we have only considered the isotropic Heisenberg exchange term in our model spin-Hamiltonian.

The estimated exchange interactions are listed in Table I. These results are fully compatible with the magnetic structure reported in³⁰. The interactions J_3 to J_6 , which play a significant role in the present context, are presented in Fig. 7 along with the zero-field magnetic structure. The strongest interaction is J_5 , imposing a perfect antiparallel alignment of the Mn³⁺ spins (represented in blue), along the direction of anisotropy. The Pr moments (in yellow) are only coupled to those Mn³⁺ through a ferromagnetic J_6 . Owing to the perfect colinearity of the Mn³⁺ and Pr³⁺ spins, it is reasonable to assume that the Pr anisotropy energy is negligible compared to J_6 . Now, it is understandable why the Mn⁴⁺ (in green) moments are not coupled to the Mn³⁺ spins. Indeed, as can be seen in Table I, J_4 is almost two orders of magnitude smaller than J_5 , excluding this path to connect the two sub-lattices. The other possible connection between Mn³⁺ dimers goes via J_3 which is nearly an order of magnitude smaller than J_5 . This interaction connects Mn⁴⁺ to two antiparallel Mn³⁺ spins. As a consequence, the two paths connecting Mn³⁺ and Mn⁴⁺ via J_3 exactly compensate each other. As for J_1 and J_2 , they couple two Mn⁴⁺ moments along c . Symmetries of the magnetic structure are shown in Fig. 7(a), resulting the magnetic space group $P_{ab}2_1a$. This space group is the same as the one reported for other members of the series, such as GdMn₂O₅¹⁵.

From the experimental results³⁰, we know that there are two distinct magnetic sublattices having separate ordering temperatures. The first one involves Mn³⁺ and Pr³⁺ spins and the second one is formed by the Mn⁴⁺ spins. The fact that these two sublattices do not order at the same temperature, indicates that there is almost no coupling between the two. That is the reason why we considered the Pr³⁺-Mn³⁺ interaction J_6 only

TABLE I. The Mn-Mn and Mn-Pr exchange interactions (in meV) obtained from the converged GGA+U calculations using the magnetic-force theorem⁵¹. The negative values imply antiferromagnetic interaction.

J_i	Ions involved	Distance (Å)	Magnitude (meV)
J_1	Mn ⁴⁺ -Mn ⁴⁺	2.95	-0.110
J_2	Mn ⁴⁺ -Mn ⁴⁺	2.74	0.182
J_3	Mn ³⁺ -Mn ⁴⁺	3.39	-0.040
J_4	Mn ³⁺ -Mn ⁴⁺	3.61	-0.004
J_5	Mn ³⁺ -Mn ³⁺	3.61	-0.205
J_6	Pr ³⁺ -Mn ³⁺	3.35	0.009

and not the Pr³⁺-Mn⁴⁺ one. As for the J_6 interaction, every Pr³⁺ ion is connected to two Mn³⁺ ions: one at 3.35 Å distance and another, at 3.80 Å distance. Our calculations show that the Pr³⁺-Mn³⁺ exchange corresponding to the distance of 3.80 Å is negligibly small due to the very large distance. In view of that, we have provided only the value of J_6 in the Table I which actually corresponds to the Pr³⁺-Mn³⁺ distance of 3.35 Å.

Interestingly, the Pr³⁺-Mn³⁺ interaction J_6 is ferromagnetic as opposed to the antiferromagnetic Gd³⁺-Mn³⁺ interaction in GdMn₂O₅¹⁵. The primary reason of this could be attributed to the difference in the fillings of the f -orbitals of these compounds. According to the extended Kugel-Khomskii model^{52,53}, the nature of the inter-atomic magnetic interaction primarily depends on three important parameters, namely (i) crystal-field splitting, (ii) effective hopping strengths between the relevant orbitals, participating in forming local magnetic moments, and (iii) the nominal fillings of those orbitals which determine whether the virtual hopping is allowed between them depending on their parallel or antiparallel alignment. The differences in the structural parameters of GdMn₂O₅ and PrMn₂O₅ will result slight differences in the first two parameter. However the most significant difference comes due to the third point: the nominal occupancy of Pr³⁺ is f^2 , while for the Gd³⁺ it is f^7 , which is exactly half-filled. It is well established that half-filled orbitals promote antiferromagnetic superexchange since virtual hopping is allowed only if they possess antiparallel alignments, making AFM ordering between Gd³⁺ and Mn³⁺ energetically favourable. Whereas for Pr³⁺, f orbitals are less than half-filled (f^2) and thus virtual hopping between Pr³⁺- f and Mn³⁺- d are allowed for both parallel and antiparallel alignments and resulting exchange comes out to be ferromagnetic. A detailed calculation based on the Kugel-Khomskii model using calculated hopping and onsite energies is outside the scope of this work.

D. Origin of the Field-Induced Ferroelectricity

On the basis of the estimated exchange interactions, we propose a possible model to couple the experimentally observed ferromagnetic component of Pr³⁺ to the induced ferroelectricity along the b direction. As mentioned, the essential components responsible for the magnetic order are J_5 connecting two Mn³⁺ spins and J_6 , connecting Mn³⁺ and Pr³⁺ spins.

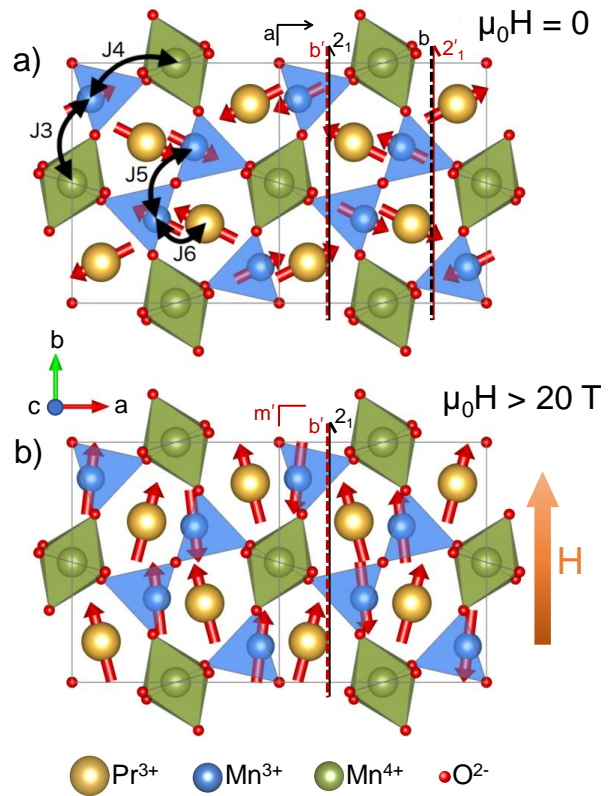


FIG. 7. (a) Schematic magnetic structure at zero field (magnetic space group $P_a b 2_1 a$)³⁰. (b) Proposed schematic magnetic structure at high field in the ferroelectric phase (magnetic space group $P b' 2_1 m'$). The amplitudes of the arrows showing the magnetic moments are not to the scale for the sake of clarity. Mn³⁺, Mn⁴⁺, and Pr³⁺ ions are represented in blue, green, and yellow, respectively.

Upon increasing the external magnetic field along the b direction, both Mn³⁺ and Pr³⁺ spins are expected to align along b . Due to the strong J_5 interaction, Mn³⁺ will persist as antiparallel dimer. This dimer will start rotating towards b as soon as the magnetic field exceeds the anisotropy energy of Mn. For the Pr³⁺ moments, there is a competition between two opposite interactions. On the one hand, the ferromagnetic interaction J_6 tries to align the Pr³⁺ spins parallel to the neighboring Mn³⁺ spins. As a consequence, Pr moments get antiferromagnetically aligned like the Mn³⁺ pairs. Now comes the Zeeman interaction term induced by the external magnetic field. It will push the Pr³⁺ spins to align along the b direction. As the XMCD results show, this happens above ~ 12 Tesla, when a ferromagnetic component from Pr moments appears along b . A compatible magnetic structure preserving the maximum of the zero-field symmetries is schematically proposed in Fig. 7(b). The magnetic symmetry operations (represented on the magnetic structure) correspond to the magnetic space group $P b' 2_1 m'$ ($P m' c' 2_1$ #26.70 in conventional setting), a subgroup of $P_a b 2_1 a$. As a result, the two Mn³⁺-Pr³⁺ pairs do not remain equivalent anymore. A slight displacement of the oxygen ions bridging the Mn³⁺ and Pr³⁺ is thus to be expected and would be different from one pair to the other. For the nearly ferromagnetically aligned Mn³⁺-Pr³⁺ pair, this dis-

placement will tend to maximize the non-frustrated J_6 interaction. On the contrary, the oxygen displacement for the nearly antiferromagnetic Mn^{3+} - Pr^{3+} pair will tend to minimize this J_6 exchange coupling. Displacements are thus different from one side to the other resulting an effective polarization along b , as observed experimentally. From a structural point of view, the average centrosymmetric space group $Pbam$ at zero field is no longer compatible. The high-field space group is thus expected to be a non-centrosymmetric subgroup of $Pbam$ and compatible with the $Pm'c'2_1$ Shubnikov group. Among the two possible subgroups fulfilling the first constraint ($Pba2$ and $Pmc2_1$), only $Pmc2_1$ allows a polarization along the b direction. Fortunately, this group also satisfies the second requirement since it is a subgroup of $Pmc2_11'$. As a conclusion, it is most likely that the high-field space group is $Pmc2_1$. This mechanism, leading to the coupling of a ferromagnetic Pr component and ferroelectricity, is thus mediated purely by a $3d$ - $4f$ super-exchange interaction. This is fundamentally different from the exchange-striction mechanism involved in the other members of the RMn_2O_5 family where a dominant $3d$ - $3d$ interaction leads to the coupling between antiferromagnetism and ferroelectricity.

According to our DFT calculation and neutron diffraction results reported earlier³⁰, in PrMn_2O_5 , the combined moment of Mn^{3+} and Mn^{4+} is much larger than the Pr^{3+} . In the field-dependent-magnetization shown in Fig. 2, only the b components of these moments contribute. The weak nature of the ferroelectricity and the measured XMCD signal signifies that the field-induced ferromagnetic component of Pr^{3+} spins along b , responsible for the breaking of centrosymmetry leading to the emergence of ferroelectricity, is rather a small fraction of its already tiny total moment of about $0.18 \mu_B$. That is why in the bulk magnetization measurement, where Pr^{3+} , Mn^{3+} , and Mn^{4+} contribute together, any possible characteristic contribution from Pr^{3+} spins in the vicinity of the field-induced polarization, was not visible in presence of a much larger background caused by the Mn moments. In contrast, an element selective technique like XMCD was able to detect successfully even the small ferromagnetic component of Pr^{3+} along the b direction. In this context, it is also important

to clarify that Fig. 7(b), which depicts our model to explain the field-induced ferroelectricity, is an exaggeration of the real scenario. To explain the symmetry breaking mechanism with better clarity, we have chosen to show the emergence of the field-induced ferromagnetic component of the Pr^{3+} spins in an amplified way compared to what one expects in reality for the present situation. This is only for the sake of better visualization of the proposed model.

III. CONCLUSION

In conclusion, the combination of electric polarization and XMCD measurements in high magnetic fields along with DFT calculations reveals the emergence of spin-driven ferroelectricity in PrMn_2O_5 under magnetic field with strong magnetoelectric coupling. In contrast to other RMn_2O_5 members ($R = \text{Nd}$ to Lu), multiferroicity in PrMn_2O_5 under magnetic field is characterized by coexisting ferroelectric and ferromagnetic components. The underlying mechanism for this spin-driven ferroelectricity involves an exchange-striction mechanism solely originated from $3d$ - $4f$ coupling as opposed to the $3d$ - $3d$ dominated multiferroicity in the other members. The observation of such a coupled ferroelectric-ferromagnetic state opens up new perspectives for technological applications. The present study evidences that there exists the possibility to stabilize a robust ferroelectric-ferromagnetic combination along with strong magnetoelectric coupling by manipulating the magnetic frustration using external parameters such as magnetic field and pressure.

ACKNOWLEDGMENT

We acknowledge the attribution of ESRF beam time under proposal HC-3783. We also acknowledge the support of the HLD at HZDR, member of the European Magnetic Field Laboratory (EMFL), and the DFG through SFB 1143 and the Würzburg-Dresden Cluster of Excellence on Complexity and Topology in Quantum Matter – *ct.qmat* (EXC 2147, Project No. 390858490).

* s.chattopadhyay@hzdr.de

¹ N. Hur, S. Park, P. A. Sharma, J. S. Ahn, S. Guha, and S.-W. Cheong, *Nature (London)* **429**, 392 (2004).

² S. W. Cheong and M. Mostovoy, *Nat. Mater.* **6**, 13 (2007).

³ M. Fiebig, T. Lottermoser, D. Meier, and M. Trassin, *Nat. Rev. Mater.* **1**, 16046 (2016).

⁴ Y. Tokunaga, S. Iguchi, T. Arima, and Y. Tokura, *Phys. Rev. Lett.* **101**, 097205 (2008).

⁵ S. Ishiwata, Y. Taguchi, H. Murakawa, Y. Onose, and Y. Tokura, *Science* **319**, 1643 (2008).

⁶ J. H. Lee, L. Fang, E. Vlahos, X. Ke, Y. W. Jung, L. F. Kourkoutis, J.-W. Kim, P. J. Ryan, T. Heeg, M. Roeckerath, V. Goian, M. Bernhagen, R. Uecker, P. C. Hammel, K. M. Rabe, S. Kamba, J. Schubert, J. W. Freeland, D. A. Muller, C. J. Fennie, P. Schiffer,

V. Gopalan, E. Johnston-Halperin, and D. G. Schlom, *Nature* **466**, 954 (2010).

⁷ C. J. Fennie, *Phys. Rev. Lett.* **100**, 167203 (2008).

⁸ N. A. Benedek and C. J. Fennie, *Phys. Rev. Lett.* **106**, 107204 (2011).

⁹ Y. Tokura, S. Seki, and N. Nagaosa, *Rep. Prog. Phys.* **77**, 076501 (2014).

¹⁰ D. Khomskii, *Physics* **2**, 20 (2009).

¹¹ S. Chattopadhyay, V. Balédent, F. Damay, A. Gukasov, E. Moshopoulou, P. Auban-Senzier, C. Pasquier, G. André, F. Porcher, E. Elkaim, C. Doubrovsky, M. Greenblatt, and P. Foury-Leykian, *Phys. Rev. B* **93**, 104406 (2016).

¹² G. Yahia, F. Damay, S. Chattopadhyay, V. Balédent, W. Peng, E. Elkaim, M. Whitaker, M. Greenblatt, M.-B. Lepetit, and P. Foury-

- Leylekian, Phys. Rev. B **95**, 184112 (2017).
- ¹³ V. Polyakov, V. Plakhty, M. Bonnet, P. Bulet, L.-P. Regnault, S. Gavrilov, I. Zobkalo, and O. Smirnov, Physica B **297**, 208 (2001).
 - ¹⁴ G. R. Blake, L. C. Chapon, P. G. Radaelli, S. Park, N. Hur, S.-W. Cheong, and J. Rodríguez-Carvajal, Phys. Rev. B **71**, 214402 (2005).
 - ¹⁵ G. Yahia, F. Damay, S. Chattopadhyay, V. Balédent, W. Peng, S. W. Kim, M. Greenblatt, M.-B. Lepetit, and P. Foury-Leylekian, Phys. Rev. B **97**, 085128 (2018).
 - ¹⁶ B. Roessli, P. Fischer, P. J. Brown, M. Janoschek, D. Sheptyakov, S. N. Gvasaliya, B. Ouladdiaf, O. Zaharko, E. Golovenchits, and V. Sanina, J. Phys.: Condens. Matter **20**, 485216 (2008).
 - ¹⁷ M. Fukunaga, Y. Sakamoto, H. Kimura, Y. Noda, N. Abe, K. Taniguchi, T. Arima, S. Wakimoto, M. Takeda, K. Kakurai, and K. Kohn, Phys. Rev. Lett. **103**, 077204 (2009).
 - ¹⁸ Y. Noda, H. Kimura, M. Fukunaga, S. Kobayashi, I. Kagomiya, and K. Kohn, J. Phys.: Condens. Matter **20**, 434206 (2008).
 - ¹⁹ M. Fukunaga, Y. Sakamoto, H. Kimura, and Y. Noda, J. Phys. Soc. Jpn. **80**, 014705 (2011).
 - ²⁰ I. Kagomiya and K. Kohn, Ferroelectrics, **219**, 169 (1998).
 - ²¹ P. G. Radaelli and L. C. Chapon, J. Phys.: Condens. Matter **20**, 434213 (2008).
 - ²² N. Hur, S. Park, P. A. Sharma, S. Guha, and S.-W. Cheong, Phys. Rev. Lett. **93**, 107207 (2004).
 - ²³ V. Balédent, S. Chattopadhyay, P. Fertey, M. B. Lepetit, M. Greenblatt, B. Wanklyn, F. O. Saouma, J. I. Jang, and P. Foury-Leylekian, Phys. Rev. Lett. **114**, 117601 (2015).
 - ²⁴ I. Kagomiya, K. Kohn, and T. Uchiyama, Ferroelectrics **280**, 131 (2002).
 - ²⁵ J. A. Alonso, M. T. Casais, M. J. Martínez-Lope, J. L. Martínez, and M. T. Fernández-Díaz, J. Phys.: Condens. Matter **9**, 8515 (1997).
 - ²⁶ B. Lorenz, Y. Q. Wang, Y. Y. Sun, and C. W. Chu, Phys. Rev. B **70**, 212412 (2004).
 - ²⁷ S. Chattopadhyay, S. Petit, E. Ressouche, S. Raymond, V. Balédent, G. Yahia, W. Peng, J. Robert, M.-B. Lepetit, M. Greenblatt, and P. Foury-Leylekian, Sci. Rep. **7**, 14506 (2017).
 - ²⁸ M. Deutsch, W. Peng, P. Foury-Leylekian, V. Balédent, S. Chattopadhyay, M. T. Fernández-Díaz, T. C. Hansen, A. Forget, D. Colson, M. Greenblatt, M.-B. Lepetit, S. Petit, and I. Mirebeau, Phys. Rev. B **98**, 024408 (2018).
 - ²⁹ S. Mansouri, S. Jandl, M. Balli, P. Fournier, B. Roberge, M. Orlita, I. A. Zobkalo, S. N. Barilo, and S. V. Shiryayev, Phys. Rev. B **98**, 205119 (2018).
 - ³⁰ C. Doubrovsky, G. André, A. Gukasov, P. Auban-Senzier, C. R. Pasquier, E. Elkaim, M. Li, M. Greenblatt, F. Damay, and P. Foury-Leylekian, Phys. Rev. B **86**, 174417 (2012).
 - ³¹ W. Peng, V. Balédent, S. Chattopadhyay, M.-B. Lepetit, G. Yahia, C. V. Colin, M. J. Gooch, C. R. Pasquier, P. Auban-Senzier, M. Greenblatt, and P. Foury-Leylekian, Phys. Rev. B **96**, 054418 (2017).
 - ³² G. Popov, M. Greenblatt, and W. McCarroll, Mater. Res. Bull. **35**, 1661 (2000).
 - ³³ B. Wanklyn, J. Mater. Sci. **7**, 813 (1972).
 - ³⁴ S. Pascarelli, O. Mathon, T. Mairs, I. Kantor, G. Agostini, C. Strohm, S. Pasternak, F. Perrin, G. Berruyer, P. Chappellet, C. Clavel, and M. C. Dominguez, J. Synchrotron Radiat. **23**, 353 (2016).
 - ³⁵ P. van der Linden, O. Mathon, C. Strohm, and M. Sikora, Rev. Sci. Instrum. **79**, 075104 (2008).
 - ³⁶ P. Frings, J. Vanacken, C. Detlefs, F. Duc, J. E. Lorenzo, M. Nardone, J. Billette, A. Zitouni, W. Bras, and G. L. J. A. Rikken, Rev. Sci. Instrum. **77**, 063903 (2006).
 - ³⁷ F. Duc, X. Fabrèges, T. Roth, C. Detlefs, P. Frings, M. Nardone, J. Billette, M. Lesourd, L. Zhang, A. Zitouni, P. Delescluse, J. Béard, J. P. Nicolin, and G. L. J. A. Rikken, Rev. Sci. Instrum. **85**, 053905 (2014).
 - ³⁸ C. Strohm, F. Perrin, M.-C. Dominguez, J. Headspith, P. vander Linden, and O. Mathon, J. Synchrotron Radiat. **18**, 224 (2011).
 - ³⁹ A. M. G. Carvalho, F. Garcia, V. S. R. de Sousa, P. J. von Ranke, D. L. Rocco, G. D. Loula, E. J. de Carvalho, A. A. Coelho, L. M. da Silva, and F. C. G. Gandra, J. Magn. Magn. Mater. **321**, 3014 (2009).
 - ⁴⁰ Y. E. Samoshkina and A. Rogalev, J. Exp. Theor. Phys. **126**, 660 (2018).
 - ⁴¹ N. Kawamura, M. Suzuki, H. Maruyama, and T. Ishikawa, J. Synchrotron Radiat. **8**, 425 (2011).
 - ⁴² C. Strohm, P. van der Linden, O. Mathon, and S. Pascarelli, Phys. Rev. Lett. **122**, 127204 (2019).
 - ⁴³ J. Chaboy, M. A. Laguna-Marco, C. Piquer, R. Boada, H. Maruyama, and N. Kawamura, J. Synchrotron Radiat. **15**, 440 (2008).
 - ⁴⁴ O. K. Andersen, Phys. Rev. B **12**, 3060 (1975).
 - ⁴⁵ J. M. Wills and B. R. Cooper, Phys. Rev. B **36**, 3809 (1987).
 - ⁴⁶ J. M. Wills, O. Eriksson, M. Alouni, and D. L. Price, *Electronic Structure and Physical Properties of Solids: The Uses of the LMTO Method* (Springer-Verlag, Berlin, 2000).
 - ⁴⁷ Y. O. Kvashnin, O. Grånäs, I. Di Marco, M. I. Katsnelson, A. I. Lichtenstein, and O. Eriksson, Phys. Rev. B **91**, 125133 (2015).
 - ⁴⁸ A. Liechtenstein, M. Katsnelson, V. Antropov, and V. Gubanov, J. Magn. Magn. Mater. **67**, 65 (1987).
 - ⁴⁹ M. I. Katsnelson and A. I. Lichtenstein, Phys. Rev. B **61**, 8906 (2000).
 - ⁵⁰ S. K. Panda, Y. O. Kvashnin, B. Sanyal, I. Dasgupta, and O. Eriksson, Phys. Rev. B **94**, 064427 (2016).
 - ⁵¹ M. I. Katsnelson and A. I. Lichtenstein, Phys. Rev. B **61**, 8906 (2000).
 - ⁵² K. I. Kugel and D. I. Khomskii, Zh. Eksp. Teor. Fiz. **64**, 1429 (1973).
 - ⁵³ K. I. Kugel and D. I. Khomskii, Sov. Phys. Uspekhi **25**, 231 (1982).